https://doi.org/10.5194/egusphere-2025-1417
Preprint. Discussion started: 17 April 2025

Extreme Concentric Gravity Waves Observed in the Mesosphere and Thermosphere Regions over Southern Brazil Associated with Fast-Moving Severe Thunderstorms

Qinzeng Li[1], Jiyao Xu[1], Yajun Zhu[1], Cristiano M. Wrasse[2], José V. Bageston[3], Wei Yuan[1], Xiao Liu[4], Weijun Liu[1], Ying Wen[5], Hui Li[1], and Zhengkuan Liu[1]

1. State Key Laboratory of Solar Activity and Space Weather, National Space Science Center, Chinese Academy of Sciences, Beijing, 100190, China
2. National Institute for Space Research, Space Weather Division, São José dos Campos, SP, Brazil
3. National Institute for Space Research, Southern Space Coordination, Santa Maria, RS, Brazil
4. School of Mathematics and Information Science, Henan Normal University, Xinxiang, 453007, China
5. College of Aviation Meteorology, Civil Aviation Flight University of China, Guanghan, 618307, China

Correspondence: Jiyao Xu (jyxu@swl.ac.cn) and Yajun Zhu (y.zhu@swl.ac.cn)

https://doi.org/10.5194/egusphere-2025-1417
Preprint. Discussion started: 17 April 2025

Abstract

Three groups of intense CGWs lasting over 10 hours were observed by an airglow imager at the Southern Space Observatory (SSO) in São Martinho da Serra (29.44°S, 53.82°W) in southern Brazil on 17-18 September 2023. These CGW events were simultaneously captured by spaceborne instruments, including the Atmospheric Infrared Sounder (AIRS) aboard Aqua, the Visible Infrared Imaging Radiometer Suite (VIIRS) onboard Suomi NPP, and the Sounding of the Atmosphere using Broadband Emission Radiometry (SABER) instrument operating on the Thermosphere-Ionosphere-Mesosphere Energetics and Dynamics (TIMED) satellite. The CGW caused significant airglow radiation perturbations exceeding 24% and the distance of the wave center movement exceeded 400 km. These CGW events were caused by fast-moving deep convections observed by Geostationary Operational Environmental Satellite-16 (GOES-16). The weaker background wind field during the spring season transition provides the necessary conditions for CGWs to propagate from the lower atmosphere to the mesopause region. The 630 nm emission images were significantly contaminated by specific OH emission bands. The same CGW event was observed propagating from the OH airglow layer to the thermospheric OI 630.0 nm airglow layer. The asymmetric propagation of CGWs in the thermosphere may be due to the vertical wavelength changes caused by the Doppler-shifting effect of the background wind field. This multi-layer ground-based and satellite joint detection of CGWs offers an excellent perspective for examining the coupling of various atmospheric layers.

https://doi.org/10.5194/egusphere-2025-1417
Preprint. Discussion started: 17 April 2025

1. Introduction

Atmospheric gravity waves (AGWs) are disturbances in the atmosphere caused by various sources, such as convection (Heale et al., 2021; Franco-Diaz et al., 2024), front/jet stream (Dalin et al., 2016; Wrasse et al., 2024), wind shear (Pramitha et al., 2015), orography forcing (Wright et al., 2017; Liu et al., 2019; Heale et al., 2020; Geldenhuys et al., 2021; Inchin et al., 2024), and air–sea interaction (Li et al., 2024). AGWs are generated when strong updrafts and downdrafts displace the stable stratification of the atmosphere. As AGWs propagate vertically from the lower atmosphere, their amplitude grows markedly owing to reduced density. When they reach mesosphere–lower thermosphere (MLT) altitudes, they become unstable and break, dissipating momentum and energy into the surrounding atmosphere (Cao and Liu, 2016; Ern et al., 2022). This energy deposition makes AGWs crucial drivers of the momentum and energy budgets in the MLT region, fundamentally governing the general circulation, thermal structure, chemical composition distribution, and transport regimes (Fritts and Alexander, 2003; Plane et al., 2023).

Among the many sources of AGWs, convective sources are particularly significant (Alexander and Holton, 2004). They can generate concentric gravity waves (CGWs), the source location of which can be readily determined by the center position. This enables point-to-point studies of their propagation characteristics. The release of latent heat in deep convection acts as a forcing mechanism (Lane et al., 2001), creating CGWs that can propagate upward into the

https://doi.org/10.5194/egusphere-2025-1417
Preprint. Discussion started: 17 April 2025

middle and upper atmosphere.

All-sky airglow imagers provide a large field of view and high-resolution observations, making them particularly suitable for observing short-period AGWs in the mesosphere and thermosphere. Through the observational data from airglow imagers, researchers can analyze the propagation characteristics of AGWs, including parameters such as horizontal wavelengths, observed periods, horizontal phase velocities and momentum fluxes (Swenson and Liu, 1998).

Although the observation of AGWs by airglow imagers has been widely documented in previous studies (Dalin et al., 2024; Nyassor et al., 2021, 2022; Suzuki et al., 2007; Vadas et al., 2012; Vargas et al., 2021; Wüst et al., 2019; Xu et al., 2015; Yue et al., 2009), dual-layer airglow observations offer a unique opportunity to simultaneously investigate CGWs in both the mesosphere and thermosphere. This configuration enables comprehensive studies of gravity wave dynamics and their role in vertical atmospheric coupling. However, due to past limitations in observational capabilities, simultaneous detection of CGWs across these two atmospheric layers was rare.

In this study, we observed multiple strong CGW events using airglow measurements, with a maximum amplitude reaching 24%, which is far higher than previously reported events (with average amplitudes of 2-3%). Through ground-based dual-layer and multi-satellite joint observations, we conducted a comprehensive analysis of these events to reveal its role in vertical energy transfer and atmospheric coupling.

https://doi.org/10.5194/egusphere-2025-1417
Preprint. Discussion started: 17 April 2025

2. Ground based Airglow Imager and Satellite observation

2.1 Airglow Imager

The airglow imager used to observe CGW is installed at the Southern Space Observatory (SSO), the National Institute for Space Research, in São Martinho da Serra (SMS) (29.44°S, 53.82°W). Figure 1 shows the location of the airglow imager station at SMS. The imager has a cooled Charge-Coupled Device (CCD) camera with a Mamiya (Focal Length = 24 mm) fish-eye lens of a 180° field of view (FOV) and a resolution of 512 × 512 pixels. The imager is equipped with a filter wheel, and the wheel rotates to observe hydroxyl (OH) (Wüst et al., 2023) broadband emission (715–930 nm, with a notch at 865.5 nm to suppress the O_2(0, 1) emission) and O(^{1}D) (630.0 nm, 2.0 nm), respectively. The time resolution of the OH airglow image is 112 seconds, while that of the OI 630 nm airglow image is 225 seconds.

https://doi.org/10.5194/egusphere-2025-1417
Preprint. Discussion started: 17 April 2025

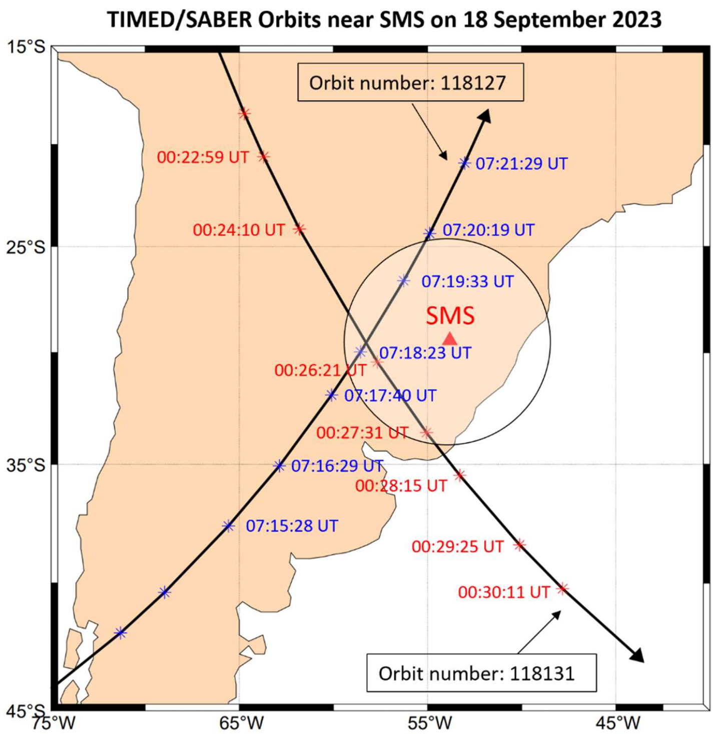

Figure 1. The location of the airglow imager station at SMS (red triangle). The circle on the map gives the effective observation ranges of OH airglow imager with a 164° field of view. The red asterisks and blue asterisks denote the TIMED/SABER ascending and descending track footprints passing over SMS on 18 September 2023, respectively.

Before effectively extracting the wave parameters, the raw airglow images need to be processed through the following steps: First, a median filter with a kernel size of 17 × 17 pixels was employed to eliminate stars from the raw images (Li et al., 2011). Second, the observed airglow intensity $I(\theta)$ from the ground is not uniform across different zenith angles. This non-uniformity is due to the van Rhijn effect. Additionally, the observed airglow intensity is influenced by atmospheric extinction, which results from absorption and scattering along the line of sight. The relationship between the $I(\theta)$ and the true airglow intensity $I_{true}(\theta)$ at zenith angle θ is

https://doi.org/10.5194/egusphere-2025-1417
Preprint. Discussion started: 17 April 2025

described by the equations (Kubota et al., 2001):

$$I(\theta) = I_{true}(\theta) \cdot 10^{-0.4aF(\theta)} = V(\theta) \cdot 10^{-0.4aF(\theta)} \cdot I(0) \quad , \tag{1}$$

$$V(\theta) = [1 - (\frac{R}{R+H}) \sin^2 \theta]^{-\frac{1}{2}} \quad , \tag{2}$$

$$F(\theta) = [\cos\theta + 0.15(93.885 - \frac{180}{\pi} \cdot \theta)^{-1.153}]^{-1} , \tag{3}$$

here, $I(0)$ represents the intensity at the zenith, R and H denote the Earth's radius and the altitude of the OH airglow layer (approximately 87 km), respectively. $V(\theta)$ is the van Rhijn correction factor, a is the atmospheric extinction coefficient, and $F(\theta)$ is an empirical function.

Third, the processed images were projected onto geographic coordinates, assuming peak emission heights of 87 km for the OH layer and 250 km for the OI 630.0 nm layer.

2.2 GOES, Aqua, Suomi NPP, and TIMED Satellite Observations

2.2.1 GOES Satellite Observations

The Geostationary Operational Environmental Satellite-16 (GOES-16), launched in November 2016, is part of the GOES-R Series. The Advanced Baseline Imager (ABI) is the primary instrument on GOES-16, providing high-resolution imagery in 16 spectral bands, including 2 visible channels, 4 near-infrared channels, and 10 infrared channels, with a temporal resolution of 10 min and a spatial resolution of 0.5–2 km. The brightness temperature (BT), derived from 10.3 μm infrared images from channel 13, is used to study the convection activities during the CGW events.

2.2.2 Aqua Satellite Observations

https://doi.org/10.5194/egusphere-2025-1417
Preprint. Discussion started: 17 April 2025

The Atmospheric Infrared Sounder (AIRS) is an infrared spectrometer and sounder onboard the NASA Aqua satellite. AIRS performs scans with a single frame image acquisition time of 6 minutes. The footprint size of AIRS is approximately 13–14 km in diameter at nadir view, and the scan swath width is around 1600–1765 km. AIRS is capable of detecting air thermal perturbations induced by GWs with vertical wavelengths longer than 10–15 km and horizontal wavelengths ~50–500 km (Hoffmann and Alexander, 2010). The radiance measurements at the 4.3 µm CO_2 fundamental emission band are particularly sensitive at altitudes around 30–40 km. In this study, the CO_2 radiance emission band with frequencies ranging between 2299.80 cm^{-1} and 2422.85 cm^{-1} is utilized to measure stratospheric air temperature perturbations.

2.2.3 Suomi NPP Satellite Observations

The Visible Infrared Imaging Radiometer Suite (VIIRS) instrument, onboard the Suomi NPP satellite, is a multispectral scanner capable of capturing high-resolution images in both visible and infrared wavelengths. The Day Night Band (DNB) of the VIIRS sensor operates in the visible/near-infrared (NIR) range, covering wavelengths from 500 to 900 nm (Miller et al., 2012), which includes three key mesospheric airglow emissions: the O(1S) line at 557.7 nm, the Na doublet at 589.0/589.6 nm, and the OH Meinel band (~600–900 nm). The sensor has a high spatial resolution of 0.375 km at nadir for its imagery bands and 0.75 km for its moderate-resolution bands. The VIIRS sensor has a wide across-track swath width of 3000 km.

https://doi.org/10.5194/egusphere-2025-1417
Preprint. Discussion started: 17 April 2025

3. Observations

3.1 Double-layer All sky Airglow Imager Observations

3.1.1 Mesospheric Concentric Gravity Waves from OH All sky imaging observation

Three groups of intense CGWs (wave packets nos. 1– 3) were captured by the OH emission channel of the airglow imager at the Southern Space Observatory (SSO) in São Martinho da Serra (29.44°S, 53.82°W) in southern Brazil on 17-18 September 2023. These events initially emerged within the imager's field of view at 22:25:02 UT on 17 September and remained continuously detectable until the cessation of observational recording at 08:35:15 UT on 18 September, thereby spanning an extended duration in excess of 10 hours. For more detailed information on the wave propagation status, please refer to the Supplement (http://doi.org/10.5446/69990, Li, 2025a). Figure 2 shows the time sequence of CGW no. 1 from 22:49:23 UT on 17 September to 03:39:31 UT on 18 September. CGW no. 1 first appeared in the southeast direction of the station.

The distinct visible concentric wavefronts radiating outward from the center (red dot in each panel) are indicative of the atmospheric response to disturbances caused by strong convection in the lower atmosphere. Interestingly, the center of CGW no. 1 continues to move eastward. Between 22:45:38 UT on 17 September and 05:26:13 UT on 18 September, the center moved approximately 436 km westward, with an average speed reaching ~65 km/h. This eastward drift of the wave's center could be indicative of the influence of prevailing wind patterns and the westward movement of the convective system itself. The horizontal wavelengths of the GWs at radii of 0–300 km (denoted by the red line in Fig. 2 at 23:39:55 UT) are measured to be (30–82)

https://doi.org/10.5194/egusphere-2025-1417
Preprint. Discussion started: 17 April 2025

± 3 km. The observed period is 9.0 ± 3.5 min, and the observed phase speed is 80–110 ms^{-1}. In the northwest direction (denoted by the red line in Fig. 2 at 00:49:11 UT), we have detected larger-scale waves with a wavelength of about 160 km, a period of approximately 16 min, and a phase speed of about 167 ms^{-1}.

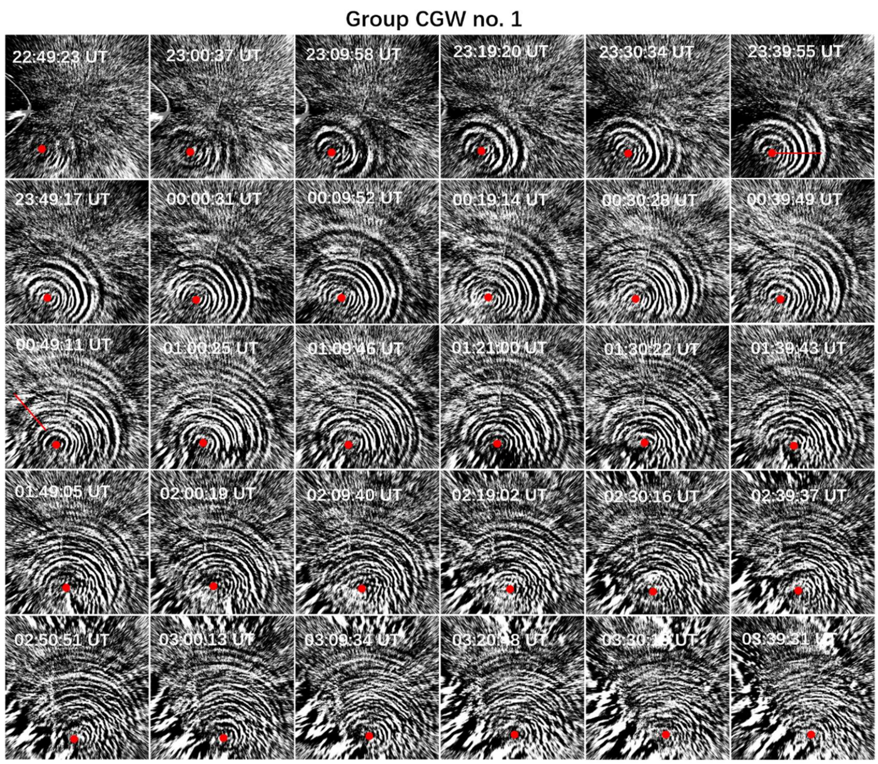

Figure 2. All-sky OH images projected onto an area of 1000 km×1000 km showing the CGW no.1 event at half-hour intervals in the SMS station on 17-18 September 2023. The red dots mark the estimated centers of the CGW.

From 02:00 UT, clouds began forming in the southwestern and western sectors of the station (see Fig. 2). By 04:00 UT, cloud formation extended to the zenith and northern sectors, persisting until ~05:30 UT. Figure 3 shows the time sequence of CGW no. 2 and CGW no. 3 from 03:58:14 UT on 17 September to 07:59:42 UT on

https://doi.org/10.5194/egusphere-2025-1417
Preprint. Discussion started: 17 April 2025

18 September. Despite cloud cover, CGW no. 2 and CGW no. 3 were observed in cloud gaps over the western sector at approximately 03:45:08 UT and 05:13:06 UT, respectively. For CGW no. 2, horizontal wavelengths range from 22 to 38 km, with a period of 7 ± 1.5 min and a phase speed of 60–78 ms^{-1}. CGW no. 3 exhibits wavelengths of 24–36 km, a period of 6.5 ± 1.0 min, and a phase speed of 72–81 ms^{-1}.

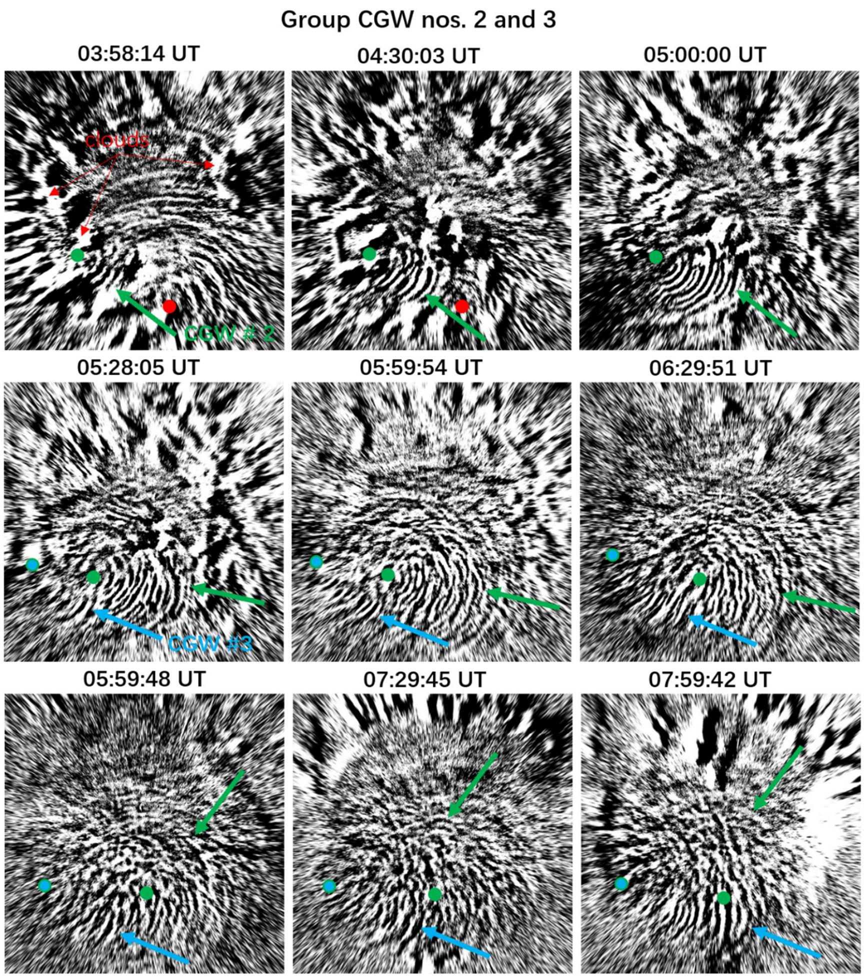

Figure 3. All-sky OH images projected onto an area of 1000 km × 1000 km showing the CGW no. 2 and CGW no. 3 events at half-hour intervals in the SMS station on 18 September 2023. The red dot marks the estimated center of the CGW no. 1, while the green and light blue dots

https://doi.org/10.5194/egusphere-2025-1417
Preprint. Discussion started: 17 April 2025

indicate the estimated centers of the CGW no. 2 and CGW no. 3, respectively.

3.1.2 Thermospheric Concentric Gravity Waves from All sky 630.0 nm imaging observation

The 630.0 nm filter used in the imager is a narrowband interference filter with a central wavelength of 630.0 nm and a full-width at half-maximum (FWHM) spectral width of 2.0 nm. Three spectral lines from the OH (9–3) band lie within the bandwidth of the 630.0 nm filter: the P2(3) line at 629.7903 nm, the P1(3) doublet at 630.6869 nm and 630.6981 nm, and the P1(2) line at 628.7434 nm (Hernandez, 1974; Burnside et al., 1977; Smith et al., 2013). To determine whether the OI 630 nm airglow image is contaminated by OH airglow emission, we project both the OH airglow image and the OI 630 nm airglow image onto the height of the OH airglow layer. We can clearly see that the OI 630 nm airglow image is contaminated by OH emission, with the CGWs observed in the OH airglow layer being superimposed onto the OI 630 nm airglow image denoted by the yellow dashed boxes in Fig. 4. Thus, we must exercise extreme caution when interpreting disturbances in the thermosphere observed at the 630 nm wavelength, particularly in the absence of concurrent OH airglow measurements to differentiate whether these disturbances are genuinely thermospheric phenomena or merely artifacts resulting from OH airglow radiation contamination. Notably, thermospheric CGWs (top panel of Fig. 4) were unambiguously observed. Their spatial mapping onto OH images confirms these signals originate from the thermosphere (bottom panel of Fig. 4), excluding OH contamination. Regarding the contamination of 630 nm images by OH emissions and the actual propagation situations of CGWs in the thermosphere, please refer to the

https://doi.org/10.5194/egusphere-2025-1417
Preprint. Discussion started: 17 April 2025

Supplement (http://doi.org/10.5446/69989, Li, 2025b).

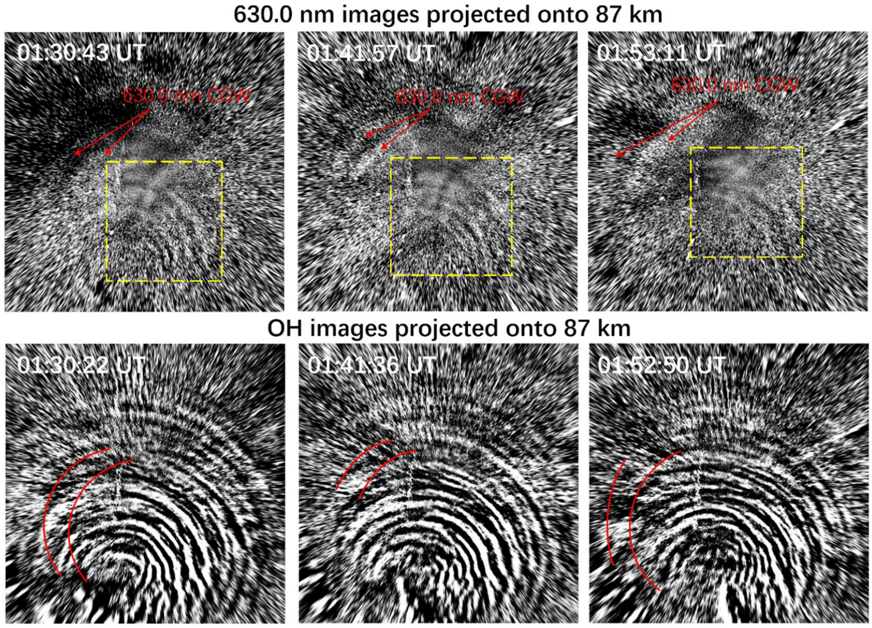

Figure 4. All-sky 630.0 nm images (top panel) and OH images (bottom panel) were both projected onto an altitude of 87 km with an area of 1000 km × 1000 km. The northeastward-propagating CGW (marked with a yellow dashed box) shows contamination from OH airglow emission. Thermospheric CGWs propagating northwestward confirmed in 630.0 nm images (top panel). The phase fronts of the thermospheric CGW are superimposed onto the OH images (bottom panel).

Figure 5 presents a series of OI 630 nm airglow emission images projected onto an altitude of 250 km. The ring-shaped arc (indicated by red arrows) propagating towards the northwest was identified, with a wavelength of approximately 165 km and a horizontal observed phase speed of about 183 ms^{-1}. The optical signatures of medium-scale traveling ionospheric disturbances (MSTIDs) in the southern hemisphere, as observed in OI 630.0 nm emission images, typically manifest as alternating dark and bright bands aligned along the northeast-southwest direction,

https://doi.org/10.5194/egusphere-2025-1417
Preprint. Discussion started: 17 April 2025

propagating in a northwestward direction (Candido et al., 2008). The MSTIDs generally exhibit full FOV coverage, traversing the entire imaging region during their propagation. However, our observations revealed that the thermospheric disturbances first emerged in the zenith region, exhibiting distinctively arcuate phase fronts, suggesting that they were excited by a quasi-point source in the lower atmosphere. The fitted center of the arc (indicated by a red dot) is located ~320 km to the southwest of the station.

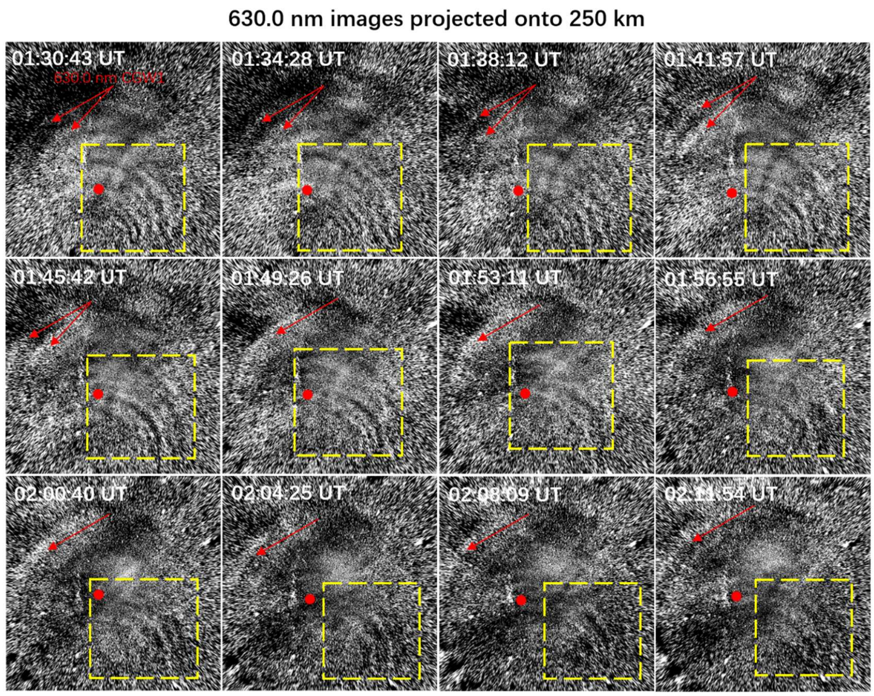

Figure 5. All-sky 630.0 nm images projected onto an area of 2000 km × 2000 km showing the thermospheric CGWs at approximately 4 min intervals in the SMS station on 18 September 2023. The red dots mark the estimated centers of the thermospheric CGW. The northeastward-propagating CGW (marked with a yellow dashed box) exhibits artifacts influenced by OH airglow emission.

https://doi.org/10.5194/egusphere-2025-1417
Preprint. Discussion started: 17 April 2025

3.2 AIRS and Sumi NPP

Figure 6 shows the AIRS 4.3 μm BT perturbation map over southern Brazil at 05:05:21 UT on 18 September 2023. The AIRS observation reveals large-scale waves propagating northwestward and westward, with a horizontal wavelength of approximately 160 km. The limited spatial resolution of AIRS restricts its detection capability for GWs with short horizontal wavelengths. The observed relatively weak fluctuations may be attributed to the decay of the convective system. Based on the stratospheric CGW's central position and propagation characteristics, we infer that this wave shares the same source with mesospheric CGW no. 1 identified in the OH all-sky images.

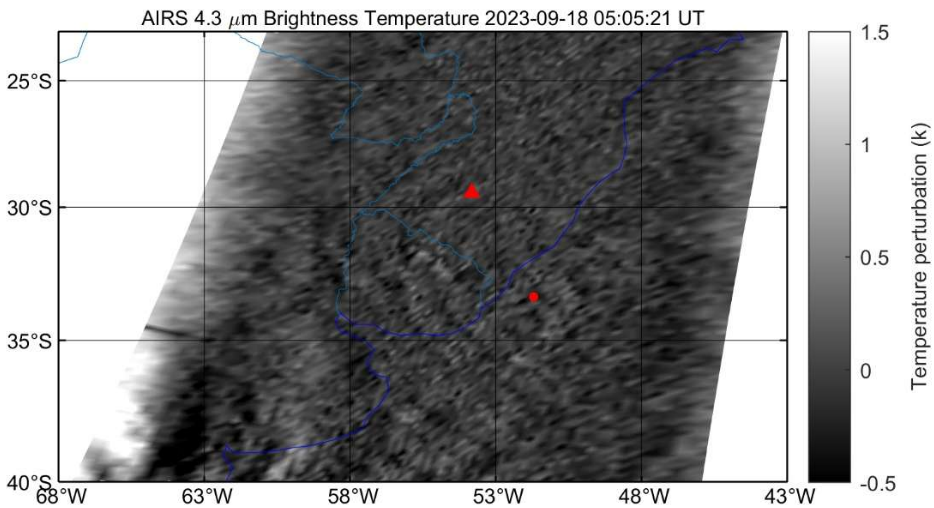

Figure 6. Aqua satellite 4.3 μm brightness temperature observations of CGWs at 05:05:21 UT on 18 September 2023. Brightness temperature is derived from 4.3 μm radiance. The red triangle and dot mark the SMS station and fitted wave center, respectively.

The Suomi-NPP satellite flew over Southern Brazil region during the progression of the CGW events. Figure 7 shows CGWs from the S-NPP VIIRS/DNB band measurements at 03:59:54 UT on 18 September 2023. The

https://doi.org/10.5194/egusphere-2025-1417
Preprint. Discussion started: 17 April 2025

horizontal wavelengths are primarily distributed within the range of (38–52) ± 3 km (indicated by a red dashed box). In the eastern direction of the small-scale wave region, large-scale waves located at (34 ° S–39 ° S, 43 ° W–46 ° W) were detected with a horizontal wavelength of approximately 154 km ± 5 km. Due to the interference of urban lighting, the CGW structures were not visible over the land.

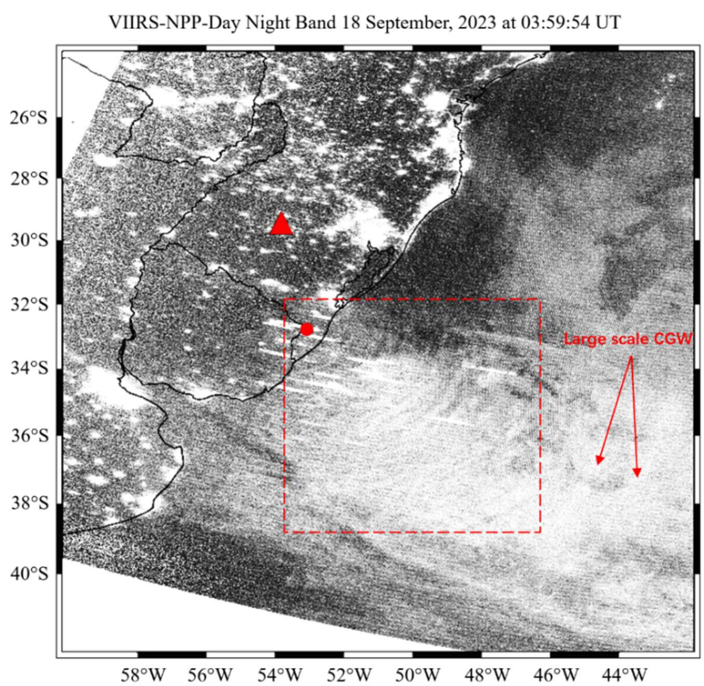

Figure 7. Suomi-NPP satellite Day Night Band radiance observations of CGWs at 03:59:54 UT on 18 September 2023. Red triangle represents the SMS station, and the red dot represents the position of the fitted center of the CGW.

3.3 GOES Observations of Convective Plumes

Figure 8 shows GOES-16 10.3 μm BT over southern Brazil from 21:00 UT to 05:30 UT on 17-18 September 2023. The first convective system initially appeared in the southwest direction of the station (indicated by the red arrow) at around

https://doi.org/10.5194/egusphere-2025-1417
Preprint. Discussion started: 17 April 2025

21:00 UT. This convective system continued to move eastward over time and had traveled approximately 400 kilometers by 05:30 UT. This eastward motion explains the observed ~436 km displacement of CGW no. 1 in the mesopause region. The second and third convective systems appeared at approximately 02:30 UT and 04:30 UT, respectively, and also moved eastward. By 06:30 UT, the three convective systems had merged together. The detailed evolution process of thunderstorm systems is provided in Supplement (http://doi.org/10.5446/69993, Li, 2025c). The spatial proximity of the three CGW centers to the initiation points of the convective systems strongly suggests these systems served as excitation sources for the CGWs detected by the airglow imager.

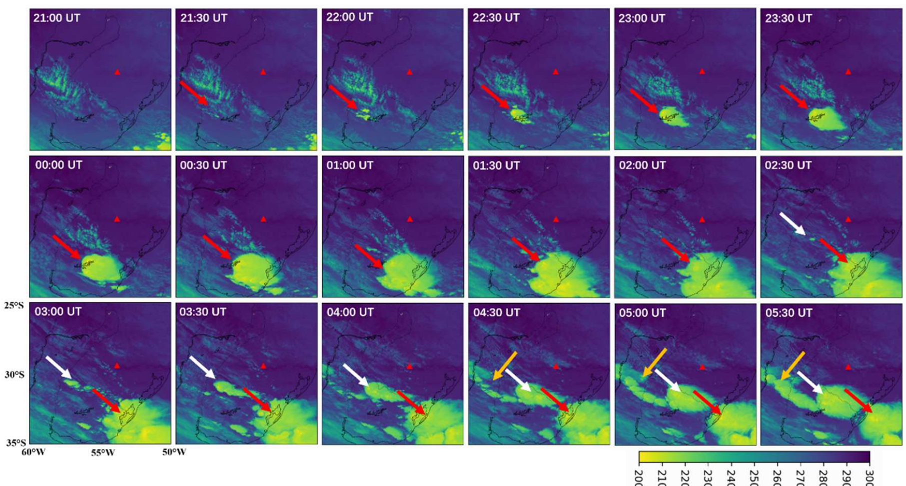

Figure 8. GOES-16 10.3 μm brightness temperature from 21:00 UT to 05:30 UT on 17-18 September 2023. The brightness temperature is derived from 10.3 μm infrared radiance data from channel 13. Red triangle represents the SMS station.

4. Results and Discussion

4.1 The characteristics of mesopause CGWs

We analyzed the background wind field above the station using a composite

https://doi.org/10.5194/egusphere-2025-1417
Preprint. Discussion started: 17 April 2025

dataset: the European Centre for Medium-Range Weather Forecasts (ECMWF) ERA5 (Hersbach et al., 2020) for 0-70 km altitude and the Horizontal Wind Model 2014 (HWM14; Drob et al., 2015) for 70-87 km altitude. Figure 9a and b show the zonal wind and meridional wind fields, respectively. Figure 9c presents a critical level filtering diagram, demonstrating how gravity waves from the lower atmosphere are prevented from reaching the mesopause region when their phase velocities fall within the prohibited range. Figure 9c presents a critical level filtering diagram, demonstrating how gravity waves from the lower atmosphere are prevented from reaching the mesopause region when their phase velocities fall within the prohibited range. The diagram reveals a maximum blocking amplitude of approximately 44 ms^{-1}. The results indicate that weaker background winds (producing smaller blocking amplitudes) enhance the vertical propagation of CGWs from the lower atmosphere to the mesosphere.

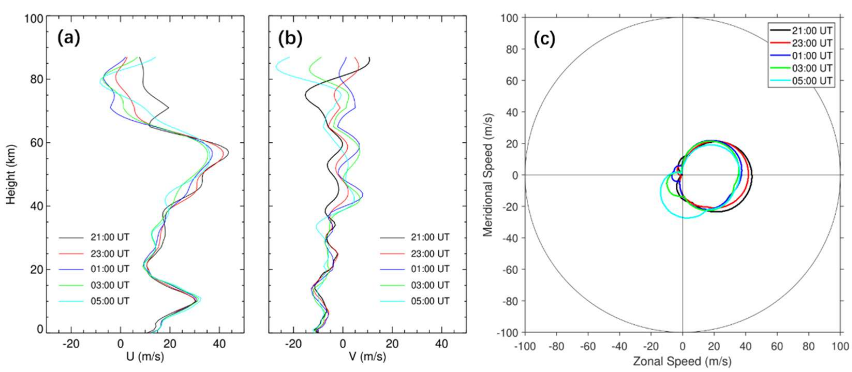

Figure 9. (a) The (a) zonal and (b) meridional wind field profiles from ERA-5 (0-70 km) and HWM14 model (70-87 km) at 21:00 UT, 23:00 UT, 01:00 UT, 03:00 UT, and 05:00 UT, respectively. (c) Two-dimensional blocking diagrams from 0 to 87 km derived from the wind profiles in (a) and (b) on 17-18 September 2023.

https://doi.org/10.5194/egusphere-2025-1417
Preprint. Discussion started: 17 April 2025

Figure 10 shows sequential cross sections of OH emission intensity perturbations perpendicular to the CGW no. 1 fronts. The wave amplitudes observed in this study exhibit significantly stronger perturbations, with a maximum relative amplitude of 24%. In contrast, previous studies have reported average amplitudes that are approximately 2% (Li et al., 2016; Tang et al., 2014; Suzuki et al., 2007). Additionally, Smith et al. (2020) reported mean-to-peak wave brightness amplitudes of 10%. We also conducted a statistical analysis of CGWs observed by a meridional airglow observation network across mainland China from September 2023 to August 2024, with data from selected stations including Daicai (25.34°N, 110.34°E), Wendeng (37.18°N, 121.79°E), Mohe (53.48°N, 122.34°E), and Naqu (31.73°N, 92.47°E). The results indicate that the average CGW amplitudes ranged between 1.7% and 2.6%.

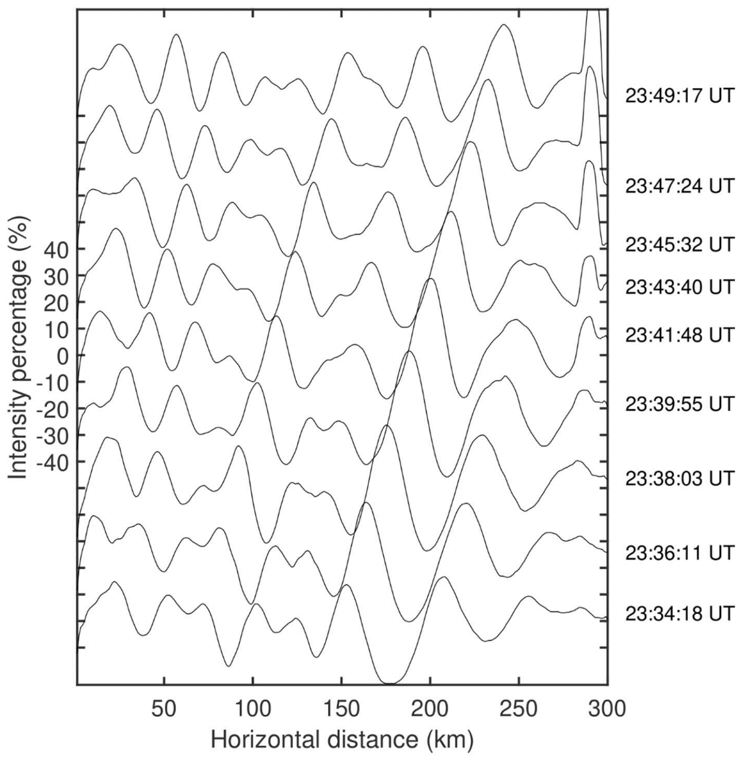

Figure 10. OH emission intensity perturbations perpendicular to the CGW no. 1 fronts (denoted by the red line in Fig. 2 at 23:39:55 UT) from 23:34:18 UT to 23:49:17 UT on 17-18 September 2023.

During the generation and propagation of CGWs, two saber orbits passed over the station and happened to be within the field of view of the airglow imager, as shown in Fig. 11. The first orbit passes over the station at approximately 00:26 UT, followed by a second orbit ~7 hours later at 07:18 UT (Fig. 1). Figure 12 presents seven OH airglow emission and temperature profiles from TIMED/SABER. We observed that the CGWs caused strong disturbances to the airglow layer. We found that the intensity of airglow emission during the first orbit (Fig. 12a) was much stronger than that during the second orbit (Fig. 12c), which

https://doi.org/10.5194/egusphere-2025-1417
Preprint. Discussion started: 17 April 2025

may suggest that the intensity of the fluctuations during the first orbit was much stronger than that during the second orbit. In addition to this, we also observed a double-peaked structure in the airglow emission layer. From the temperature profiles (Fig. 12b and d), we have detected a rich spectrum of vertically propagating waves with vertical wavelengths between 5 km and 20 km, which consists with concurrent airglow and satellite observations of upward-propagating CGWs.

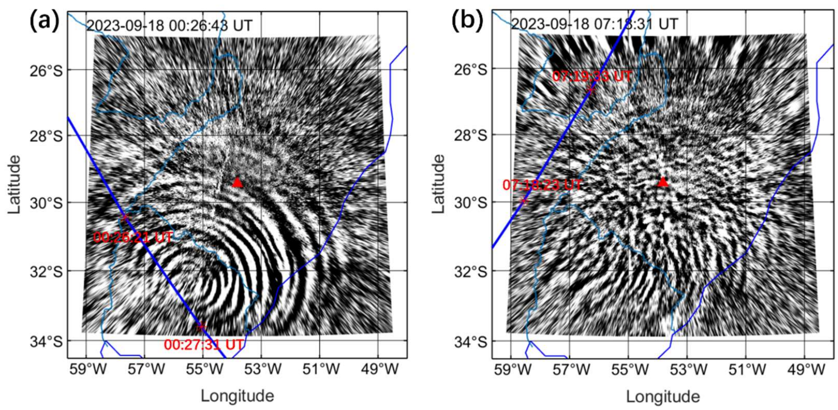

Figure 11. Simultaneous observations of CGWs using ground-based all-sky airglow imager and TIMED/SABER satellite measurements. The red triangle marks the location of the SMS station.

https://doi.org/10.5194/egusphere-2025-1417
Preprint. Discussion started: 17 April 2025

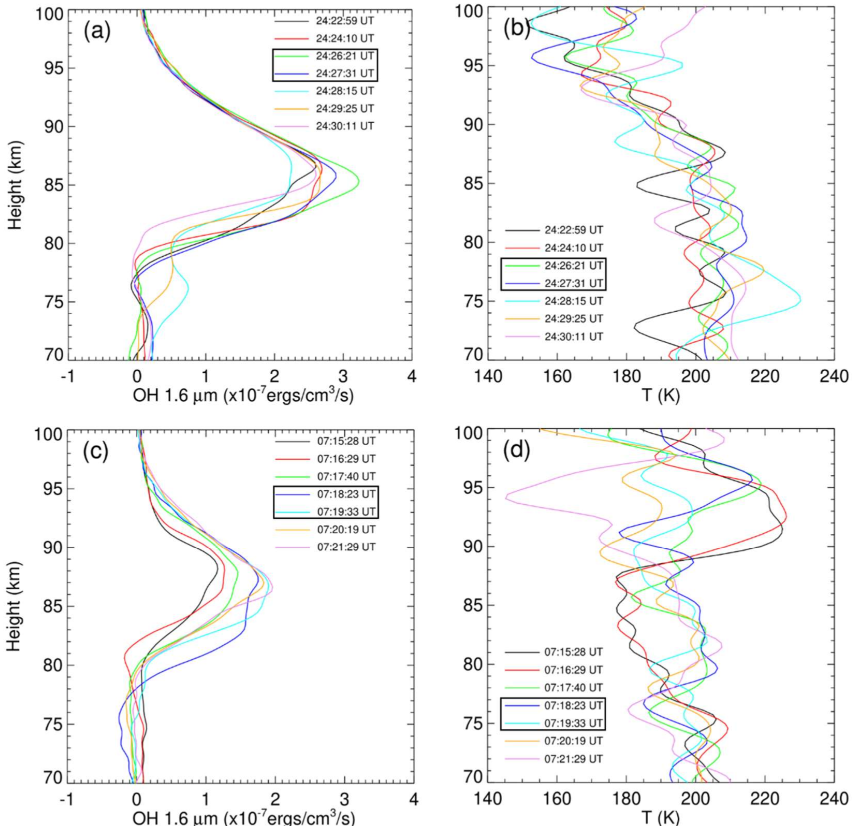

Figure 12. TIMED/SABER (a) OH 1.6 µm emission and (b) temperature profiles (ascending track), and (c) OH 1.6 µm emission and (d) temperature profiles (descending track) on 18 September 2023. Boxed profiles correspond to the satellite's passage through the airglow imager's effective FOV (see Fig. 11).

We can use airglow imaging observations to estimate gravity wave flux (F_M). The F_M (Swenson and Liu, 1998; Swenson et al., 1999) are expressed as

$$F_M = \frac{1}{2}\frac{g^2}{N^2}\frac{m}{k}\frac{\omega^2}{N^2}\left(\frac{I'}{\overline{I}}\right)^2\frac{1}{CF^2}(m^2 \cdot s^{-2}), \quad (4)$$

where $CF = 3.5-(3.5-0.1)\exp[-0.0055(\lambda_z - 6\mathrm{km})^2]$ is cancellation factor. λ_z is the vertical wavelength. I' is the perturbed airglow intensity. $\overline{I}$ is the averaged airglow intensity. N is the Brunt-Väisälä frequency derived from TIMED/SABER

https://doi.org/10.5194/egusphere-2025-1417
Preprint. Discussion started: 17 April 2025

observations. $k = \frac{2\pi}{\lambda_h}$ is the horizontal wave number. λ_h is the horizontal wavelength derived from airglow images. $m = \frac{2\pi}{\lambda_z}$ is the vertical wave number derived from the GW dispersion relation (Hines, 1960)

$$m^2 = \frac{N^2}{(c-u)^2} - k^2 - \frac{1}{4H^2} \quad , \tag{5}$$

where c is the observed horizontal phase speed of the wave, u is the wind speed in the wave direction derived from meteor radar, H is the scale height from the SABER temperature profile.

Figure 13 shows the calculated vertical flux of the horizontal momentum flux of CGWs from 22:00 to 09:00 UT on 17-18 September 2023. We found that CGW no. 1 produced substantially stronger momentum flux (peak value >450 m^2s^{-2}) compared to CGW no. 2 and CGW no. 3, which showed similar but weaker magnitudes. These values markedly exceed previous measurements (typically 1-17 m^2s^{-2} in Li et al. 2016 and Tang et al. 2014) and even surpass the intense event (decaying from 300 to 150 m^2s^{-2}) reported by Smith et al. (2020). The results reveal that the fast-moving thunderstorm systems generated exceptionally powerful wave activity, transporting substantial momentum and energy into the MLT region. These events represent the most intense vertical transport cases ever recorded, demonstrating remarkable wave coupling between the lower and upper atmosphere.

https://doi.org/10.5194/egusphere-2025-1417
Preprint. Discussion started: 17 April 2025

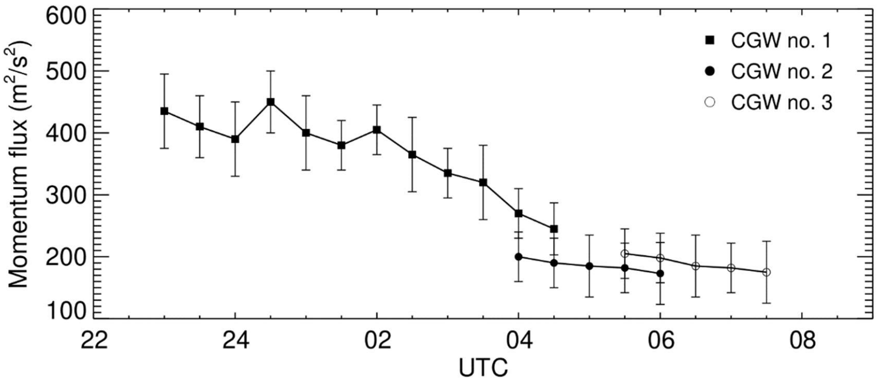

Figure 13. Temporal evolution of vertical flux of horizontal momentum from 22:00 to 09:00 UT on 17-18 September 2023.

We use the following vertical group velocity equation to estimate the time required for the CGWs generated by the convective systems to propagate to the MLT region.

$$C_{gz} = \frac{\Delta z}{\Delta t} = -\frac{Nkm}{(k^2 + m^2)^{3/2}}, \tag{6}$$

where Δz and Δt are the vertical distance and propagation time of the CGWs from troposphere to airglow layer, respectively. α is zenith angle between the vertical altitude and propagation direction of the CGWs phase fronts. The vertical group velocities of CGW no. 1, CGW no. 2, and CGW no. 3 are estimated to be 31–37 ms^{-1}, 24–30 ms^{-1}, and 26–29 ms^{-1}, respectively. This implies that the time taken for CGW no. 1, CGW no. 2, and CGW no. 3 to reach the OH airglow layer (87 km) is approximately 32-39 min, 40-50 min, and 41-46 min, assuming the excitation height of CGWs is 15 km.

4.2 The characteristics of thermospheric CGWs

We further investigated the propagation characteristics of thermospheric CGWs.

https://doi.org/10.5194/egusphere-2025-1417
Preprint. Discussion started: 17 April 2025

The vertical group velocity of the thermospheric gravity waves can be estimated using the following approximate relationship: $C_{gz} \sim -\frac{N}{k}\cos^2\alpha\sin\alpha$. The zenith angle α is approximately 61° from Fig. 14a. The buoyancy frequency N is estimated to be 2π/10.35 min at the thermosphere height of 250 km, which is derived from the empirical neutral atmosphere model (NRLMSISE-00) (Picone et al., 2002). The horizontal wavenumber k=2π/165 km. The estimated vertical group velocity is about 54 ± 6 ms^{-1}. Based on the vertical group velocity, we find that the time taken for the gravity waves to propagate from the OH layer and the tropopause region to the thermosphere is approximately 50 ± 5 min and 73 ± 8 min, respectively. Given the thermospheric arrival time of 01:41:57 UT (Fig. 14a), the CGWs were likely excited near the tropopause (~15 km altitude) at approximately 00:28:57 UT (Fig. 14c), passed through the OH layer (~87 km altitude) between approximately 00:46:57 UT and 00:56:57 UT. Notably, GWs with comparable scales were observed in the OH layer at around 00:54:48 UT (Fig. 14b), which suggests that they might be the same wave.

As mentioned above, the observed thermospheric CGW exhibits an asymmetric structure, appearing as arc-shaped waves only in the eastern and northeastern directions. This asymmetry can be attributed to the Doppler effect of the background wind field, which influences gravity wave detection through wave cancellation. GWs propagating against background wind are Doppler shifted to a larger vertical wavelength, and increased chance of observation (Li et al., 2016). These GWs suffer little cancelation can be easily detected by airglow imager GWs observations. GWs

https://doi.org/10.5194/egusphere-2025-1417
Preprint. Discussion started: 17 April 2025

propagating along background wind are Doppler shifted to a smaller vertical wavelength, causing the wave amplitude to become invisible. As illustrated in Fig. 14d, the eastward zonal wind at 250 km altitude reaches ~90 ms^{-1}. This strong eastward wind likely suppresses the visibility of eastward-propagating thermospheric CGWs in airglow imaging. The Doppler shift reduces their vertical wavelengths, causing them to fall below the detection threshold of the vertically integrated airglow observations.

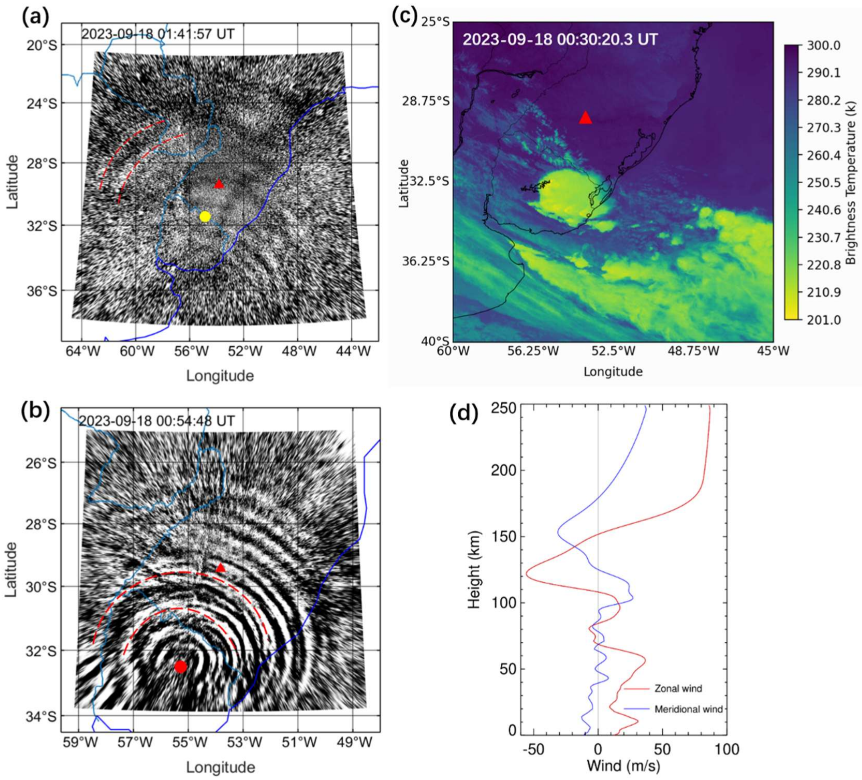

Figure 14. (a) All-sky 630.0 nm imaging observation of thermospheric CGW at 01:41:57 UT on 18 September 2023. The yellow dot marks the estimated center of the thermospheric CGW. (b) All-sky OH imaging observation of mesospheric CGW at 00:54:48 UT on 18 September 2023. The red dot marks the estimated center of the mesospheric CGW. (c) GOES-16 10.3 μm

https://doi.org/10.5194/egusphere-2025-1417
Preprint. Discussion started: 17 April 2025

brightness temperature at 00:20:20 UT on 17-18 September 2023. (d) Wind profiles from ERA-5 (0-70 km) and HWM14 (70-250 km) averaged between 01:00 UT and 02:00 UT on 18 September 2023.

5. Conclusions

In this study, we investigated intense CGWs using coordinated dual-channel airglow observations (630.0 nm and OH bands) from the Southern Space Observatory (SSO) in São Martinho da Serra, Brazil, complemented by multi-satellite measurements during 17-18 September 2023. The key findings are summarized as follows:

These unprecedented CGWs exhibited remarkable persistence (>10 hours), extreme amplitude perturbations (>24%), and substantial wave-center movement (>400 km). These wave events were unambiguously linked to fast-moving convective systems observed by GOES-16. The weaker background wind field during the spring season transition was identified as a crucial factor that allowed CGWs to propagate from the lower atmosphere to the MLT region.

The OI 630 nm airglow observations were substantially contaminated by overlapping OH Meinel band emissions (715-930 nm). This contamination leads to spurious apparent vertical coupling, as mesospheric gravity waves (CGWs) are artificially projected onto the thermospheric OI 630 nm emission layer. This cross-layer aliasing effect necessitates rigorous validation protocols when interpreting putative thermospheric disturbances at 630 nm, particularly requiring spatio-temporally collocated OH airglow measurements (e.g., OH (9–3) bands) to discriminate genuine dynamical processes from lower atmospheric contamination

https://doi.org/10.5194/egusphere-2025-1417
Preprint. Discussion started: 17 April 2025

artifacts.

The asymmetric propagation of CGWs in the thermosphere was attributed to variations in vertical wavelength induced by the Doppler effect of background winds. Specifically, the eastward zonal wind at 250 km altitude, reaching approximately 90 ms^{-1}, reduced the vertical wavelength of eastward-propagating CGWs, making them undetectable in airglow imaging observations due to vertical integration effects.

This study reveals intense CGWs originating from deep convective systems that play a dominant role in transferring wave energy and momentum from the troposphere to the MLT region. These waves exhibited exceptional characteristics including prolonged persistence, extreme amplitude perturbations, and significant horizontal movement, demonstrating their substantial impact on atmospheric dynamics and space weather. Our coordinated multi-instrument approach, combining dual-channel airglow observations with satellite measurements, provides crucial insights into wave propagation while addressing the challenges of cross-layer contamination in OI 630 nm emissions. These findings significantly advance our understanding of gravity wave dynamics in the upper atmosphere and establish an improved observational framework for studying atmospheric coupling processes.

Data availability. The airglow data are available from the web page of the Estudo e Monitoramento Brasileiro do Clima Espacial (EMBRACE/INPE) at http://www2.inpe.br/climaespacial/portal/en (EMBRACE, 2024). TIMED/SABER data are accessible from http://saber.gats-inc.com/data.php (Mlynczak et al., 2023).

The ERA5 reanalysis data are available for downloaded from the Copernicus Climate Change Service Climate Data Store at https://doi.org/10.24381/cds.bd0915c6 (Hersbach et al., 2023). The GOES-16 ABI L1b radiances data are accessible from https://www.ncdc.noaa.gov/airs-web/search (Schmit et al., 2017). AIRS radiance data radiances data are accessible from https://disc.gsfc.nasa.gov/datasets/AIRIBRAD_005/summary (AIRS project, 2007). VIIRS DNB data are distributed by the NOAA Comprehensive Large Array-data Stewardship System (CLASS)(https://www.aev.class.noaa.gov/saa/products/welcome;jsessionid=C3562F228661BE845B176C9AE2714AE6) (Miller et al., 2012).

Video supplement. Extreme mesospheric concentric gravity waves from OH airglow observations over Southern Brazil is available for view (http://doi.org/10.5446/69990, Li, 2025a). Thermospheric concentric gravity waves from OI 630 nm airglow observations over Southern Brazil is available for view (http://doi.org/10.5446/69989, Li, 2025b). Fast-moving severe thunderstorms over Southern Brazil from GOES-16 observations is available for view (http://doi.org/10.5446/69993, Li, 2025c).

Author contributions. QL conceived the idea of the article and wrote the manuscript. JX carried out the analysis of the AIRS and NPP data. XL contributed to the analysis of the SABER data. YZ contributed to the processing of ECMWF data. WY, XL, HL, and ZL contributed to the data interpretation and manuscript preparation. CMW and

https://doi.org/10.5194/egusphere-2025-1417
Preprint. Discussion started: 17 April 2025

JVB revised the manuscript. All authors discussed the results and commented on the paper.

Competing interests. The contact author has declared that none of the authors has any competing interests.

Acknowledgements. We thank the National Natural Science Foundation of China (grant nos. 42374205). The authors thank the Estudo e Monitoramento Brasileiro do Clima Espacial (EMBRACE/INPE) for the provision of the all-sky data. We acknowledge the use of data from the Chinese Meridian Project. We appreciate the TIMED/SABER team for providing the temperature and emission intensity data. We also thank the European Centre for Medium-Range Weather Forecasts (ECMWF) for the provision of the ERA5 data and Geostationary Operational Environmental Satellite (GOES) team for the ABI L1b radiances data. We also thank the NASA Goddard Earth Sciences Data Information and Services Center (GES DISC) for providing AIRS data and NOAA Comprehensive Large Array-data Stewardship System (CLASS) for providing Day Night Band data.

Financial support. This research has been supported by the National Natural Science Foundation of China (grant nos. 42374205) and the Specialized Research Fund of National Space Science Center, Chinese Academy of Sciences (grant no. E4PD3010).

https://doi.org/10.5194/egusphere-2025-1417
Preprint. Discussion started: 17 April 2025

This work has been supported by the B-type Strategic Priority Program of CAS (grant no. XDB0780000). The project has also been supported by the Specialized Research Fund for State Key Laboratories.

References

AIRS project: AIRS/Aqua L1B Infrared (IR) geolocated and calibrated radiances V005, Greenbelt, MD, USA, Goddard Earth Sciences Data and Information Services Center (GES DISC), [data set], https://doi.org/10.5067/YZEXEVN4JGGJ, 2007.

Alexander, M. J., and Holton, J. R.: On the spectrum of vertically propagating gravity waves generated by a transient heat source, Atmos. Chem. Phys., 4, 923–932, https://doi.org/10.5194/acp-4-923-2004, 2004.

Burnside, R. G., Meriwether, J. W., and Torr, M. R.: Contamination of ground-based measurements of OI (6300 Å) and NI (5200 Å) airglow by OH emissions, Planet. Space. Sci., 25(10), 985–988, https://doi.org/10.1016/0032-0633(77)90012-5, 1977.

Candido, C. M. N., Pimenta, A. A., Bittencourt, J. A., and Becker-Guedes, F.: Statistical analysis of the occurrence of medium-scale traveling ionospheric disturbances over Brazilian low latitudes using OI 630.0 nm emission all-sky images, Geophys. Res. Lett., 35, L17105, https://doi.org/10.1029/2008GL035043, 2008.

Cao, B., and Liu, A. Z.: Intermittency of gravity wave momentum flux in the mesopause region observed with an all-sky airglow imager, J. Geophys. Res. Atmos., 121, https://doi.org/10.1002/2015JD023802, 2016.

Dalin, P., Gavrilov, N., Pertsev, N., Perminov, V., Pogoreltsev, A., Shevchuk, N., Dubietis, A., Völger, P., Zalcik, M., Ling, A., Kulikov, S., Zadorozhny, A.,

https://doi.org/10.5194/egusphere-2025-1417
Preprint. Discussion started: 17 April 2025

Salakhutdinov, G., and Grigoryeva, I.: A case study of long gravity wave crests in noctilucent clouds and their origin in the upper tropospheric jet stream, J. Geophys. Res.-Atmos., 121, 14102–14116, https://doi.org/10.1002/2016JD025422, 2016.

Dalin, P., Brändström, U., Kero, J., Voelger, P., Nishiyama, T., Trondsen, T., Wyatt, D., Unick, C., Perminov, V., Pertsev, N., and Hedin, J.: A novel infrared imager for studies of hydroxyl and oxygen nightglow emissions in the mesopause above northern Scandinavia, Atmos. Meas. Tech., 17, 1561–1576, https://doi.org/10.5194/amt-17-1561-2024, 2024.

Drob, D. P., Emmert, J. T., Meriwether, J. W., Makela, J. J., Doornbos, E., Conde, M., Hernandez, G., Noto, J., Zawdie, K. A., McDonald, S. E., Huba, J. D., and Klenzing, J. H.: An update to the Horizontal Wind Model (HWM): The quiet time thermosphere, Earth and Space Science, 2, 301–319, https://doi.org/10.1002/2014EA000089, 2015.

EMBRACE: Estudo e Monitoramento Brasileiro do Clima Espacial–EMBRACE/INPE, http://www2.inpe.br/climaespacial/portal/en (last access: 15 September 2024), 2024.

Ern, M., Preusse, P., and Riese, M.: Intermittency of gravity wave potential energies and absolute momentum fluxes derived from infrared limb sounding satellite observations, Atmos. Chem. Phys., 22, 15093–15133, https://doi.org/10.5194/acp-22-15093-2022, 2022.

Franco-Diaz, E., Gerding, M., Holt, L., Strelnikova, I., Wing, R., Baumgarten,

https://doi.org/10.5194/egusphere-2025-1417
Preprint. Discussion started: 17 April 2025

G., and Lübken, F.-J.: Convective gravity wave events during summer near 54° N, present in both AIRS and Rayleigh–Mie–Raman (RMR) lidar observations, Atmos. Chem. Phys., 24, 1543–1558, https://doi.org/10.5194/acp-24-1543-2024, 2024.

Fritts, D. C., and Alexander, M. J.: Gravity wave dynamics and effects in the middle atmosphere, Reviews of Geophysics, 41(1), https://doi.org/10.1029/2001RG000106, 2003.

Geldenhuys, M., Preusse, P., Krisch, I., Zülicke, C., Ungermann, J., Ern, M., Friedl-Vallon, F., and Riese, M.: Orographically induced spontaneous imbalance within the jet causing a large-scale gravity wave event, Atmos. Chem. Phys., 21, 10393–10412, https://doi.org/10.5194/acp-21-10393-2021, 2021.

Heale, C. J., Bossert, K., Vadas, S. L., Hoffmann, L., Dornbrack, A., Stober, G., Snively, J. B., and Jacobi, C.: Secondary gravity waves generated by breaking mountain waves over Europe, J. Geophys. Res.-Atmos., 125, e2019JD031662, https://doi.org/10.1029/2019JD031662, 2020.

Heale, C. J., Inchin, P. A., and Snively, J. B.: Primary Versus Secondary Gravity Wave Responses at F-Region Heights Generated by a Convective Source, J. Geophys. Res.-Space, 127, e2021JA029947, https://doi.org/10.1029/2021JA029947, 2021.

Hernandez, G.: Contamination of the OI (3 P2–1 D2) emission line by the (9–3) band of OH X2 II in high-resolution measurements of the night sky, J.

Geophys. Res., 79, 1119–1123, https://doi.org/10.1029/JA079i007p01119, 1974.

Hersbach, H., Bell, B., Berrisford, P., Hirahara, S., Horányi, A., Muñoz-Sabater, J., Nicolas, J., Peubey, C., Radu, R., Schepers, D., Simmons, A., Soci, C., Abdalla, S., Abellan, X., Balsamo, G., Bechtold, P., Biavati, G., Bidlot, J., Bonavita, M., De Chiara, G., Dahlgren, P., Dee, D., Diamantakis, M., Dragani, R., Flemming, J., Forbes, R., Fuentes, M., Geer, A., Haimberger, L., Healy, S., Hogan, R. J., Hólm, E., Janisková, M., Keeley, S., Laloyaux, P., Lopez, P., Lupu, C., Radnoti, G., deRosnay, P., Rozum, I., Vamborg, F., Villaume, S., and Thépaut, J. N.: The ERA5 global reanalysis, Q. J. Roy. Meteor. Soc., 146, 1999–2049, https://doi.org/10.1002/qj.3803, 2020.

Hersbach, H., Bell, B., Berrisford, P., Biavati, G., Horányi, A., Muñoz Sabater, J., Nicolas, J., Peubey, C., Radu, R., Rozum, I., Schepers, D., Simmons, A., Soci, C., Dee, D., and Thépaut, J.- N.: ERA5 hourly data on pressure levels from 1940 to present, Copernicus Climate Change Service (C3S) Climate Data Store (CDS) [data set], https://doi.org/10.24381/cds.bd0915c6, 2023.

Hines, C. O.: Internal atmospheric gravity waves at ionospheric heights. Can. J. Phys., 38(11), 1441–1481, https://doi. org/10.1139/p60-150, 1960.

Hoffmann, L., and Alexander, M. J.: Occurrence frequency of convective gravity waves during the North American thunderstorm season, J. Geophys. Res., 115, D20111, https://doi.org/10.1029/2010JD014401, 2010.

Inchin, P. A., Bhatt, A., Bramberger, M., Chakraborty, S., Debchoudhury, S., and

https://doi.org/10.5194/egusphere-2025-1417
Preprint. Discussion started: 17 April 2025

Heale, C.: Atmospheric and ionospheric responses to orographic gravity waves prior to the December 2022 cold air outbreak, Journal of Geophysical Research: Space Physics, 129, e2024JA032485. https://doi.org/10.1029/2024JA032485, 2024.

Kubota, M., Fukunishi, H., and Okano, S.: Characteristics of medium-and large-scale TIDs over Japan derived from OI 630- nm nightglow observation, Earth Planets Space, 53, 741–751. https://doi.org/10.1186/BF03352402, 2001.

Lane, T. P., Reeder, M. J., and Clark, T. L.: Numerical modeling of gravity wave generation by deep tropical convection, J. Atmos. Sci., 58, 1249–1274, https://doi.org/10.1175/1520- 0469(2001)0582.0.CO;2, 2001.

Li, Q., Xu, J., Liu, X., Yuan, W., and Chen, J.: Characteristics of mesospheric gravity waves over the southeastern Tibetan Plateau region, Journal of Geophysical Research: Space Physics, 121(9), 9204–9221, https://doi.org/10.1002/2016JA022823, 2016.

Li, Q., Xu, J., Gusman, A. R., Liu, H., Yuan, W., Liu, W., Zhu, Y., and Liu, X.: Upper-atmosphere responses to the 2022 Hunga Tonga–Hunga Ha′apai volcanic eruption via acoustic gravity waves and air–sea interaction, Atmos. Chem. Phys., 24, 8343–8361, https://doi.org/10.5194/acp-24-8343-2024, 2024.

Li, Q.: Extreme mesospheric concentric gravity waves from OH airglow observations over Southern Brazil, TIB AV-Portal [video],

https://doi.org/10.5194/egusphere-2025-1417
Preprint. Discussion started: 17 April 2025

http://doi.org/10.5446/69990, 2025a.

Li, Q.: Thermospheric concentric gravity waves from OI 630 nm airglow observations over Southern Brazil, TIB AV-Portal [video], http://doi.org/10.5446/69990, 2025b.

Li, Q.: Fast-moving severe thunderstorms over Southern Brazil from GOES-16 observations, TIB AV-Portal [video], https://doi.org/10.5446/69993, 2025c.

Li, Z., Liu, A. Z., Lu, X., Swenson, G. R., and Franke, S. J.: Gravity wave characteristics from OH airglow imager over Maui, J. Geophys. Res., 116, D22115, https://doi.org/10.1029/2011JD015870, 2011.

Liu, X., Xu, J. Y., Yue, J., Vadas, S. L., and Becker, E.: Orographic primary and 309 secondary gravity waves in the middle atmosphere from 16-year SABER 310 observations, Geophysical Research Letters, 46, 4512–4522, https:// 311 doi.org/10.1029/2019GL082256, 2019.

Miller, S. D., Mills, S. P., Elvidge, C. D., Lindsey, D. T., Lee, T. F., and Hawkins, J. D.: Suomi satellite brings to light a unique frontier of nighttime environmental sensing capabilities, Proc. Natl. Acad. Sci. U.S.A., 109(39), 15,706–15,711, https://doi.org/10.1073/pnas.1207034109, 2012 (data available at https://www.aev.class.noaa.gov/saa/products/welcome;jsessionid=C3562F228661BE845B176C9AE2714AE6, last access: 15 December 2024).

Mlynczak, M. G., Marshall, B. T., Garcia, R. R., Hunt, L., Yue, J., Harvey, V. L., Lopez-Puertas, M., Mertens, C., and Russell, J.: Algorithm stability and the long-term geospace data record from TIMED/SABER, Geophys. Res. Lett., 50, 1–7, https://doi.org/10.1029/2022GL102398, 2023 (data available at http://saber.gats-inc.com/data.php, last access: 10 December 2024).

Nyassor, P. K., Wrasse, C. M., Gobbi, D., Paulino, I., Vadas, S. L., Naccarato, K. P., Takahashi, H., Bageston, J. V., Figueiredo, C. A. O. B., and Barros, D.: Case Studies on Concentric Gravity Waves Source Using Lightning Flash Rate, Brightness Temperature and Backward Ray Tracing at São Martinho da Serra (29.44° S, 53.82° W), J. Geophys. Res.-Atmos., 126, e2020JD034527, https://doi.org/10.1029/2020JD034527, 2021.

Nyassor, P. K., Wrasse, C. M., Paulino, I., São Sabbas, E. F. M. T., Bageston, J. V., Naccarato, K. P., Gobbi, D., Figueiredo, C. A. O. B., Ayorinde, T. T., Takahashi, H., and Barros, D.: Sources of concentric gravity waves generated by a moving mesoscale convective system in southern Brazil, Atmos. Chem. Phys., 22, 15153–15177, https://doi.org/10.5194/acp-22-15153- 2022, 2022.

Plane, J. M. C., Gumbel, J., Kalogerakis, K. S., Marsh, D. R., and von Savigny, C.: Opinion: Recent developments and future directions in studying the mesosphere and lower thermosphere, Atmos. Chem. Phys., 23, 13255–13282, https://doi.org/10.5194/acp-23-13255-2023, 2023.

Pramitha, M., Venkat Ratnam, M., Taori, A., Krishna Murthy, B. V., Pallamraju, D., and Vijaya Bhaskar Rao, S.: Evidence for tropospheric wind shear excitation of high-phase-speed gravity waves reaching the mesosphere

https://doi.org/10.5194/egusphere-2025-1417
Preprint. Discussion started: 17 April 2025

using the ray-tracing technique, Atmos. Chem. Phys., 15, 2709–2721, https://doi.org/10.5194/acp-15- 2709-2015, 2015.

Picone, J. M., Hedin, A. E., Drob, D. P., and Aikin, A. C.: NRLMSISE-00 empirical model of the atmosphere: Statistical comparisons and scientific issues, J. Geophys. Res., 107, 1468, https://doi.org/10.1029/2002JA009430, 2002.

Schmit, T. J., Griffith, P., Gunshor, M. M., Daniels, J. M., Goodman, S. J., and Lebai, W. J.: A Closer Look at the ABI on the GOES-R Series. Bulletin of the American Meteorological Society, 98(4), 681–698, https://doi.org/10.1175/bams-d-15-00230.1, 2017 (data available at https://www.ncdc.noaa.gov/airs-web/search, last access: 10 December 2024).

Smith, S. M., Setvák, M., Beletsky, Y., Baumgardner, J., and Mendillo, M.: Mesospheric gravity wave momentum flux associated with a large thunderstorm complex, Journal of Geophysical Research: Atmospheres, 125, e2020JD033381, https://doi.org/ 10.1029/2020JD033381, 2020.

Smith, S. M., Vadas, S. L., Baggaley, W. J., Hernandez, G., and Baumgardner, J.: Gravity wave coupling between the mesosphere and thermosphere over New Zealand, Journal of Geophysical Research-Space Physics, 118(5), 2694–2707, https://doi.org/10.1002/jgra.50263, 2013.

Suzuki, S., Shiokawa, K., Otsuka, Y., Ogawa, T., Nakamura, K., and Nakamura, T.: A concentric gravity wave structure in the mesospheric airglow images, Journal of Geophysical Research, 112(D2), D02102. https://doi.org/10.1029/2005JD006558, 2007.

Swenson, G. R., and Liu, A. Z.: A model for calculating acoustic gravity wave energy and momentum flux in the mesosphere from OH airglow, Geophysical Research Letters, 25, 477–480, https://doi.org/10.1029/98GL00132, 1998.

Swenson, G. R., Haque, R., Yang, W., and Gardner, C. S.: Momentum and energy fluxes of monochromatic gravity waves observed by an OH imager at Starfire Optical Range, New Mexico, J. Geophys. Res., 104(D6), 6067–6080, https://doi.org/10.1029/1998JD200080, 1999.

Tang, Y., Dou, X., Li, T., Nakamura, T., Xue, X., Huang, C., Manson, A., Meek, C., Thorsen, D., and Avery, S.: Gravity wave characteristics in the mesopause region revealed from OH airglow imager observations over Northern Colorado, J. Geophys. Res. Space Physics, 119, 630–645, https://doi.org/10.1002/2013JA018955, 2014.

Vadas, S., Yue, J., and Nakamura, T.: Mesospheric concentric gravity waves generated by multiple convective storms over the North American Great Plain, J. Geophys. Res., 117, D07113, https://doi.org/10.1029/2011JD017025, 2012.

Vargas, F., Chau, J. L., Charuvil Asokan, H., and Gerding, M.: Mesospheric gravity wave activity estimated via airglow imagery, multistatic meteor radar, and SABER data taken during the SIMONe–2018 campaign, Atmos.

Chem. Phys., 21, 13631–13654, https://doi.org/10.5194/acp-21-13631-2021, 2021.

Wrasse, C. M., Nyassor, P. K., da Silva, L. A., Figueiredo, C. A. O. B., Bageston, J. V., Naccarato, K. P., Barros, D., Takahashi, H., and Gobbi, D.: Studies on the propagation dynamics and source mechanism of quasi-monochromatic gravity waves observed over São Martinho da Serra (29° S, 53° W), Brazil, Atmos. Chem. Phys., 24, 5405–5431, https://doi.org/10.5194/acp-24-5405-2024, 2024.

Wright, C. J., Hindley, N. P., Hoffmann, L., Alexander, M. J., and Mitchell, N. J.: Exploring gravity wave characteristics in 3-D using a novel S-transform technique: AIRS/Aqua measurements over the Southern Andes and Drake Passage, Atmos. Chem. Phys., 17, 8553–8575, https://doi.org/10.5194/acp-17-8553-2017, 2017.

Wüst, S., Bittner, M., Espy, P. J., French, W. J. R., and Mulligan, F. J.: Hydroxyl airglow observations for investigating atmospheric dynamics: results and challenges, Atmos. Chem. Phys., 23, 1599–1618, https://doi.org/10.5194/acp-23-1599-2023, 2023.

Wüst, S., Schmidt, C., Hannawald, P., Bittner, M., Mlynczak, M. G., and Russell III, J. M.: Observations of OH airglow from ground, aircraft, and satellite: investigation of wave-like structures before a minor stratospheric warming, Atmos. Chem. Phys., 19, 6401– 6418, https://doi.org/10.5194/acp-19-6401-2019, 2019.

https://doi.org/10.5194/egusphere-2025-1417
Preprint. Discussion started: 17 April 2025

Xu, J., Li, Q., Yue, J., Hoffmann, L., Straka, W. C., Wang, C., Liu, M., Yuan, W., Han, S., Miller, S. D., Sun, L., Liu, X., Liu, W., Yang, J., and Ning, B.: Concentric gravity waves over northern China observed by an airglow imager network and satellites, J. Geophys. Res.-Atmos., 120, 11058–11078, https://doi.org/10.1002/2015JD023786, 2015.

Yue, J., Vadas, S. L., She, C. Y., Nakamura, T., Reising, S. C., Liu, H. L., and Li, T.: Concentric gravity waves in the mesosphere generated by deep convective plumes in the lower atmosphere near Fort Collins, Colorado, Journal of Geophysical Research, 114, D06104, https://doi.org/10.1029/2008JD011244, 2009.